FULL ARTICLE

Transmission of classically entangled beams through mouse brain tissue

Sandra Mamani[1] | Lingyan Shi[1,2] | Tahmid Ahmed[3] | Romir Karnik[4] | Adrián Rodríguez-Contreras[5] |
Daniel Nolan[6] | Robert Alfano[1]*

[1]Institute for Ultrafast Spectroscopy and Lasers, Department of Physics, The City College of the City University of New York, New York, New York

[2]Department of Chemistry, Columbia University, New York, New York

[3]Brooklyn Technical High School, Brooklyn, New York

[4]The Bronx High School of Science, Bronx, New York

[5]Department of Biology, The City College of the City University of New York, New York, New York

[6]Corning Research and Development Corporation, Sullivan Park, Corning, NY, USA

*Correspondence
Robert Alfano, Institute for Ultrafast Spectroscopy and Lasers, Department of Physics, The City College of the City University of New York, 160 Convent Avenue, New York, NY 10031.
Email: ralfano@ccny.cuny.edu

Light transmission of Laguerre-Gaussian vector vortex beams in different local regions in mouse brain tissue is investigated. Transmittance is measured in the ballistic and diffusive regions with various polarizations states and orbital angular momentums (OAM). The transmission change observed with structured light other than linear polarization is attributed to chiroptical phenomena from the chiral brain media and the handedness of the light. For instance, classically entangled beams showed higher transmittance and constant value dependency on OAM modes than linear modes did. Also, circular polarization beam transmittance showed strong increase with topical charge OAM (ℓ), which could be attributed to chiroptical effect.

KEYWORDS

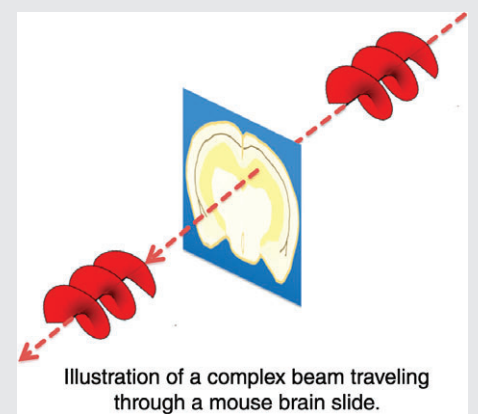chirality, classical entanglement, light scattering, mouse brain, OAM beam, polarization, vector beam

Illustration of a complex beam traveling through a mouse brain slide.

1 | INTRODUCTION

In optical imaging, light's salient properties such as polarization, wavelength, and spatial modes play an important role for imaging in scattering media. Structured light is an active research topic in various fields in classical and quantum entanglement. Scattering blurs images and the degree of scattering depends on wavelength. The polarization becomes randomized due to scattering. Large particles scatter the light mainly in the forward direction unlike small particles that scatter in all directions with regard to the wavelength of light [1].

Also, blue light (shorter wavelength) scatters more than red light (longer wavelength), resulting in a blue sky as well as red horizons during sunset and sunrise. The scattering intensity varies as the inverse of wavelength to power $n > 2$ for Mie scattering.

Due to inhomogeneous make up of tissue from particles and structure, tissues are highly scattering media. In this case, the wavelength plays a key role for biological media; the scattering reduces as wavelength enters the NIR (690-900 nm) and in SWIR (1000-2500 nm). The optimum window in SWIR for deep imaging is the golden window (1600-1850 nm) in the brain [2].

Moreover, polarization plays an important role since it can affect the depth at which the beam travels. For example, it is known that circular polarized light goes deeper than linear polarized light [3]. Depending on scattering unit size, the polarization retains optical memory [4]. A Laguerre-Gaussian (LG) beam [5], which is a vortex beam, can carry different types of polarization (linear, circular, radial and azimuthal) along with a phase front characterized by an orbital angular momentum (OAM) of ℓ value. Light beams with spatially inhomogeneous profile of polarization are referred to as vector beams. The various spatial modes, such as the radial, have non-separable parts for circular polarization and OAM. The combination of polarization and spatial modes leads to classical entanglement—Forbes group [6] used classical entangled vector beams for better imaging in turbulent media. The key characteristic of vector beams such as radial and azimuthal combines polarization and spatial modes, which are non-separable and are entangled. These characteristics are not only unique to quantum entanglement but also applicable to vector beams that are classically entangled locally [6–9]. Moreover, the characteristic of non-separability in vector beams is of great interest not just in optical imaging but in optical communication as well since its polarization degree of freedom and spatial mode are being explored to encode information [7, 10].

Furthermore, according to theory [11], higher ℓ values show more transmittance, resulting in a better penetrating ability, hence less optical density (OD) and less scattering observed. As the light pulse enters a highly scattering media such as tissue, it breaks up into three main components: ballistic, snake, and diffusive. The ballistic component retains original properties of the light since it is coherently scattered in the forward direction, while the diffusive component becomes randomized and wanders about the media. The snake component is slightly scattered in the forward direction, traveling over a shorter path length and retaining initial information [12].

This study focuses on the transmission of LG vector vortex beams through mouse brain tissue in the ballistic ($z < l_{tr}$) and diffusive ($z > l_{tr}$) regions, where z is the thickness of the turbid media and l_{tr} is the transport mean free path [13]. Different types of polarizations at different special locations of the mouse brain at various thicknesses are investigated to demonstrate the role of classical entanglement in potentially improving imaging with higher flux of photons in the classical limit.

The brain is a biological tissue made up of neurons and axons in tree—like structure. Neurons are organized by integrated networks of protein polymers, which are considered a chiral medium. This chiral medium will interact with the electromagnetic field of light by changing its state of polarization; this effect makes the brain a chiral bio-plasma [14]. Structured vector light is expected to interact with chiral matter by coupling with electric dipole, magnetic dipole and

quadrupole moments and transitions from Fermi Golden Rule [15–18]. The underlying unique and complex structure and properties make the brain a "smart tissue"; due to this heterogeneity in the brain, different regions could show dissimilar effects. Electric quadrupole interactions enable the twisted light to twist more with a wavelength to be involved with local electronic transitions. Therefore, we decided to focus on main brain regions such as the cortex, white matter and hippocampus. White and gray (cortex and hippocampus) matter are considered major regions of the central nervous system. These are regions mainly affected by neurodegenerative diseases such as Alzheimer's and multiple sclerosis among others [19, 20].

In this experiment, these brain regions are examined to determine whether there are special maze pathways in brain tissue for photons to propagate as vortex LG OAM beams. The polarization and OAM value ℓ are changed for each localized spatial region. Our goals are to observe if there is a direct proportionality between the OAM(ℓ) and the transmission, and chiroptical interactions between a targeted region in the brain and each polarization used. Chiroptical effects involve interplay of chirality of molecular and electromagnetic radiation to produce energy shifts to the handedness of circular polarized photons such as circular dichroism in solids, liquids and biofluids [14–18].

Our work motivated from the past work done by Shi and colleagues [21], where mouse brain transmission with LG was also only done for linear polarized light with no classical entanglement. No transmission effect was observed for linear polarization (LP) on OAM (ℓ). The polarized states are further expanded here to include classical entangled beams with circular, radial, and azimuthal polarization for OAM of LG beams. One can expect that circular polarization and entangled light beams will affect the photons absorption rates. The use of classical entanglement is that it operates locally and uses a high flux of photons in contrast to quantum entanglement that uses a single low photon number non-locally [22].

1.1 | Four States of polarization and spatial modes

Vector beams are spatial modes with varying states of polarization. Radial polarized (RP) and azimuthal polarized (AP) modes can produce stronger longitudinal electric and magnetic field components upon focusing. RP can also generate smaller spot size upon focusing by a high NA objective lens to form imaging in nano scale. Most importantly, RP and AP are non-separable beams (mixed states) in space and polarization, being classically entangled.

The following represents the four polarization states in Dirac notation and Jones vector [6, 8, 9, 23–26]. Equation (1) is a linear polarization, which is a state representation of right and left circular polarization.

$$|\text{LP}\rangle = |\text{RH}\rangle + |\text{LH}\rangle. \tag{1}$$

Circular polarization can be written in a more general form as shown in Eq. (2) as a pure state:

$$|\text{CP}\rangle = \cos\varphi|x\rangle \pm \sin\varphi e^{i\delta}|y\rangle, \tag{2}$$

where φ represents the azimuthal phase at $\pi/4$ with respect to the x-axis and δ, which is the complex phase taken at $\pi/2$, $|+\rangle$ and $|-\rangle$ are two general eigenvector states, which represent two column vectors $\binom{1}{0}$ and $\binom{0}{1}$.

Equation (3) represents right-handed circular polarization:

$$|\text{RH}\rangle = \frac{1}{\sqrt{2}}\binom{1}{-i} = = \frac{1}{\sqrt{2}}[|+\rangle - i|-\rangle]. \tag{3}$$

Equation (4) represents left-handed circular polarization:

$$|\text{LH}\rangle = \frac{1}{\sqrt{2}}\binom{1}{i} = = \frac{1}{\sqrt{2}}[|+\rangle + i|-\rangle]. \tag{4}$$

LG beams with circular polarization (pure states) are represented by Eq. (5):

$$|\ell\rangle|\text{RH}\rangle; |-\ell\rangle|\text{RH}\rangle; \text{and } |\ell\rangle|\text{LH}\rangle; |-\ell\rangle|\text{LH}\rangle, \tag{5}$$

where ℓ represents the OAM value.

Equation (6) shows radial polarization (classical entangled local state) with spatial and polarization:

$$|\text{RP}\rangle = \frac{1}{\sqrt{2}}\binom{\cos\varphi}{\sin\varphi} \to \frac{1}{\sqrt{2}}\left[e^{i\varphi}\binom{1}{-i} + e^{-i\varphi}\binom{1}{i}\right] =$$
$$= \frac{1}{\sqrt{2}}\left[e^{i\varphi}|\text{RH}\rangle + e^{-i\varphi}|\text{LH}\rangle\right]. \tag{6}$$

The notation in Eq. (6) shows that radial polarization is a superposition of two states $|\text{RH}\rangle$ and $|\text{LH}\rangle$. The exponent is a variation phase and is a unique characteristic of vortex beams.

LG beams with radial polarization are represented by Eq. (7), which is a mixed state:

$$|\text{LG}_{\text{RP}}\rangle \frac{1}{\sqrt{2}}[|-\ell\rangle|\text{LH}\rangle + |\ell\rangle|\text{RH}\rangle]. \tag{7}$$

Equation (8) represents azimuthal polarization (classical entangled local mixed state) with spatial and polarization:

$$|\text{AP}\rangle = \frac{1}{\sqrt{2}}\binom{-\sin\varphi}{\cos\varphi} \to \frac{1}{\sqrt{2}}\left[e^{i(\varphi+\pi/2)}\binom{1}{-i} + e^{-i(\varphi+\pi/2)}\binom{1}{i}\right] =$$
$$= \frac{1}{\sqrt{2}}\left[e^{i(\varphi+\pi/2)}|\text{RH}\rangle + e^{-i(\varphi+\pi/2)}|\text{LH}\rangle\right] \tag{8}$$

The notation in Eq. (8) shows that azimuthal polarization is also made of a superposition of $|\text{RH}\rangle$ and $|\text{LH}\rangle$. However, the variation phase has an extra $\pi/2$ phase shift.

LG beams with azimuthal polarization are represented by Eq. (9), which is a mixed state:

$$|\text{LG}_{\text{AP}}\rangle \frac{-i}{\sqrt{2}}[|-\ell\rangle|\text{LH}\rangle - |\ell\rangle|\text{RH}\rangle]. \tag{9}$$

Equations (10) and (11) represent beams with higher order of radial and azimuthal polarization:

$$|\text{HLG}_{\text{RP}}\rangle = \frac{1}{\sqrt{2}}\left[e^{i(2\ell_{\text{VR}} + \ell_{\text{SLM}})\varphi}|\text{RH}\rangle + e^{-i(2\ell_{VR} - \ell_{SLM})\varphi}|\text{LH}\rangle\right], \tag{10}$$

$$|\text{HLG}_{\text{AP}}\rangle = \frac{1}{\sqrt{2}}\left[e^{i[(2\ell_{\text{VR}} + \ell_{\text{SLM}})(\varphi + \pi/2)]}|\text{RH}\rangle + e^{-i[(2\ell_{\text{VR}} - \ell_{\text{SLM}})(\varphi + \pi/2)]}|\text{LH}\rangle\right], \tag{11}$$

where $2\ell_{\text{VR}} \pm \ell_{\text{SLM}}$ represents the total OAM(ℓ).

In order to generate radially and azimuthally polarized beams with higher OAM values, we combined in a tandem application (see Section 2) a vortex retarder (VR) and spatial light modulator (SLM) as shown mathematically in Eqs. (10) and (11). A vortex retarder acts as a half wave retarder that generates LG beams with $(\ell) = 2\ell_{\text{VR}}\hbar$, where ℓ_{VR} is the topological charge imparted from a vortex retarder and $\hbar$ is Planck's constant divided by 2π. The spatial light modulator is another apparatus used to generate LG beams with $(\ell) = \ell_{\text{SLM}}\hbar$, where ℓ_{SLM} can take any positive or negative integer value, just as the ℓ_{VR}. The combination of both apparatuses gives a higher order of OAM (ℓ) values [27].

It is well known that as a photon (ω) enters a material it becomes dressed by refractive index, n (ω). The photon can excite electrons causing vibrations, which couple to the media quasi-particles to become a coupled quasi-particle or a polariton depending on how ω gets close to the resonance frequency ω_o. These quasi-particles commonly become one of the following: optical phonon, exciton, plasmon and/or magnon-polariton. The dielectric media can be represented by Lorentz dipole with resonance ω_o from quasi-particle interaction with photon of angular frequency ω. In addition, depending on ω being close to ω_o, one can obtain the condition of generating precursors of Sommerfeld (high frequency) or Brillouin (low frequency) types. It is known that photons can couple to plasmons, optical photons, magnons and excitons. The photon excitations become a quasi particle from the interactions and become dressed [28, 29]. Quasi particles can be made up of three sub entities: Holons (charge), Orbitons and Spinons. A photon quasi-particle can be split into spin and orbital in OAM and SAM optical beams.

Special paths may exist in the brain for photons to travel through [30]. The brain is very different from other body organs such as the breast, cervix, skin and kidney. It has special tree-like structure with connections of 86 billion neurons and axon branches [31] to store and retrieve information from memory. There are six different types of nerve cells in the central nervous system, which are nourished and

protected by neuroglia or glial cells (glue like media) [32]. The photons enter the brain and travel in this maze, interacting with existing chiral proteins and lipid molecules. There is a possible existence of optical waveguide fiber–like lanes in the brain from microtubules that the photon may take upon exiting [30, 33–35]. If these classical non-separable structure modes exist in the chiral brain, they would increase the transmission and retain coherence. These special photon quasi-particles can be more transmitted and retain the input characteristics and be entangled with sister photons, which can be called C-on (classical mode) in contrast to Q-on (quantum mode) of single photons. We have introduced a new quasi-particle photon that differs from pure states of CP and LP in the brain, and defined this new quasi-particle of the classical (C-on) entangled photon, which is radially and azimuthally mixed and non-separable coupled and quantum entangled Bell photons traveling in the brain (Q-On). This paper on transmission in brain tissue for OAM and SAM and vector beams shines light on C-on existence in the brain.

2 | METHODS

2.1 | Experimental set-up

Figure 1 shows the experimental setup where a He-Ne laser of 5 mW at 633 nm was used as a light source, focusing onto a single-mode optical fiber (SMOF). The output beam from the optical fiber passed through a collimator and illuminated the spatial light modulator (SLM), which was set at reflection mode. The SLM produced LG
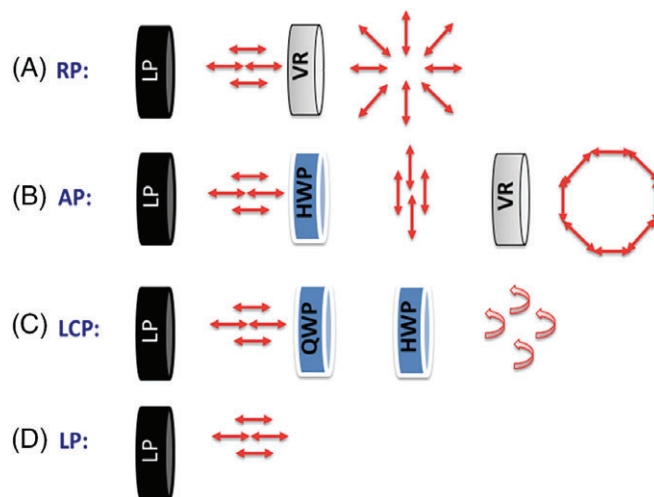

FIGURE 2 Generation of four different polarization states. RP, radial polarization; AP, azimuthal polarization; LCP, left circular polarization; LP, linear polarization. (A and B) vector beams; (C and D) scalar beams. VR, vortex retarder; HWP, half wave plate, QWP, quarter wave plate

beams of different ℓ values that were generated by different forked diffraction patterns. A first lens was used to collimate the first order diffraction through a 400-µm aperture, decreasing the beam's overall exposure to light. A second lens was then used to re-collimate the beam. The beam then propagated through various types of polarization states (see Section 2.2, Figure 2). Then the LG beam with specific polarization went through a healthy mouse brain sample. Finally, the beam went through a 4f imaging system constituting of two lenses ($L_3 = 5$ cm, $L_4 = 10$ cm). A CCD camera detected the output.
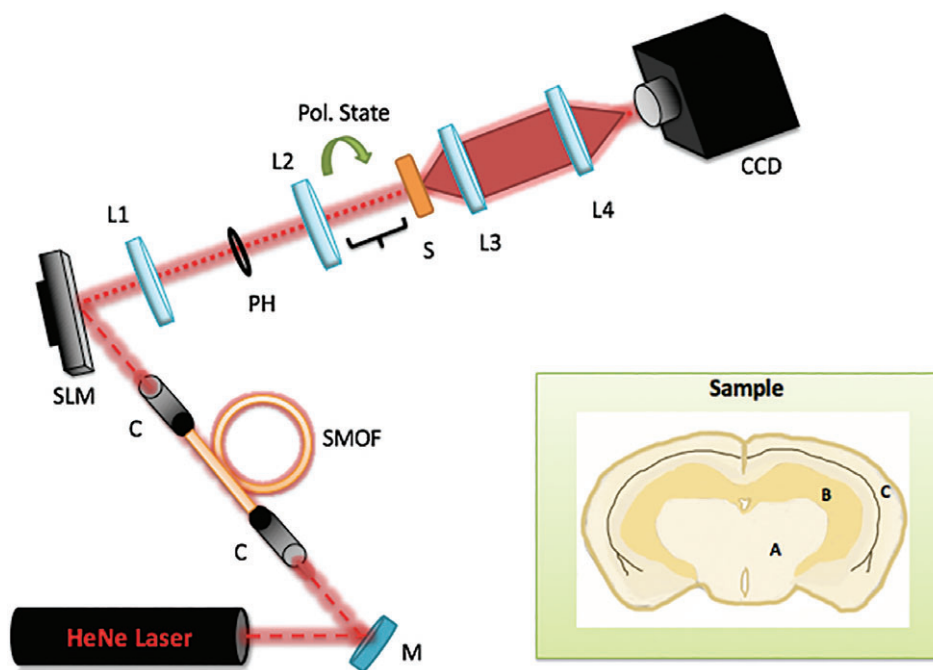

FIGURE 1 General experimental setup. M, mirror; C, collimator; SMOF, single mode optical fiber; SLM, spatial light modulator; L, lenses; PH, pinhole; Pol. State, four different types of polarization; S, sample; CCD, charge coupled device camera. Sample parts: A, hippocampus; B, white matter; C, cortex

2.2 | Generating different states of vortex beams

To generate vector vortex beams with various OAM values, we combined a spatial light modulator (SLM) with a vortex retarder (VR). A SLM is a phase and amplitude modulator that generates vortex beams by inputting computer generated holograms onto the phase of the SLM. A vortex retarder (VR) is a spatially inhomogeneous phase retarder. The one used in the experiment is a $\ell = 1$ vortex retarder, which is polarization dependent. In the experiment (Figure 1), the SLM will generate a vortex beam with $\ell_{total - SLM}$ value. Then, the beam will go through a set of polarizers and then through the VR (Figure 2A,B) which will be combined with $\ell_{total - VR}$, creating a vortex beam with a total value of OAM. In order to generate the vector beam with a specific polarization, we fixed the fast axis of the VR to one direction. Then, we sent in different orientation of linear polarization with respect to the axis of the VR. To generate a radially polarized beam, a horizontally polarized beam has to go through a vortex retarder (VR) with respect to its optical axis (Figure 2A). One way to characterize a radially polarized beam is by inserting a linear polarizer after the VR and as a result two lobes will be formed (Figure 3A, second
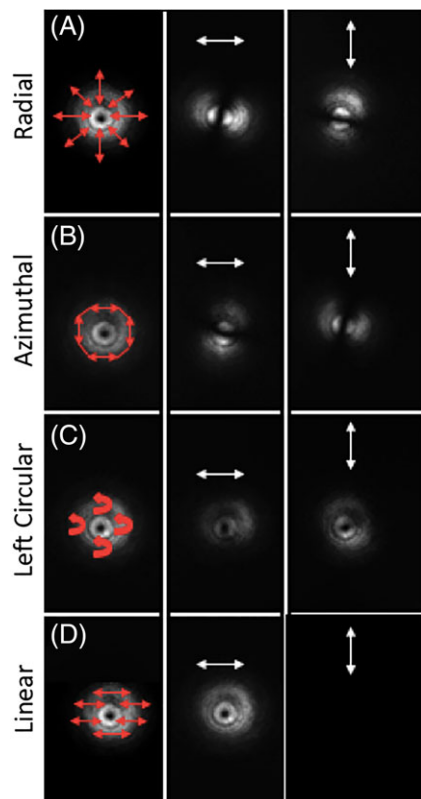
and third columns). This is also a way to characterize a vector vortex beam since one of its characteristics is that their helical mode decomposition result is dependent on the input polarization. To generate an azimuthally polarized beam, a vertically polarized (horizontally polarized beam going into a half wave plate) beam needs to go through the VR with respect to its optical axis (Figure 2B). In this case if we place a linear polarizer in front of the VR, the two lobes will form again but now shifted 90° from the radial polarization (Figure 3B, second and third columns).

Finally, to generate scalar vortex beams we only used the SLM set at different ℓ values. To generate the circularly polarized light, a linear polarized beam needs to pass through a quarter wave plate at an angle of 45°. Also a half wave plate can be used to generate a left circularly polarized beam (Figure 2C). In this case if we put a linear analyzer afterwards, the two lobes will not form anymore and instead we will see a decrease of intensity (Figure 3C, second and third columns). Therefore, circular polarization proves to be a scalar beam, whose helical mode is independent of polarization. In the case of linear polarization, a horizontally polarized beam was used (Figure 2D). Additionally, for the linear polarization, the maximum intensity is observed when the analyzer is set horizontally and no intensity when analyzer is set vertically (Figure 3D, second and third columns).

Figure 3 shows different types of vortex beams with their intensity profile characterized by an analyzer. For the vector beams (Figure 3A,B), the SLM was set to $\ell = 0$ while the VR was always contributing an $\ell = 1$. In this case the vector beams generated a superposition of ± 1 giving a total OAM value of $\ell = 0$. For the left circular and linear polarized beam, the SLM was set to $\ell = 1$ (Figure 3C,D). For higher values of vector or scalar beams the SLM can be set to higher values of ℓ.

FIGURE 3 Characterization of vortex beams. For this case the total OAM is $\ell = 1$ (A) Radial polarization with its electric field pointing on the radial direction from the center of the beam. (B) Azimuthal polarization with its electric field tangential to the beam. (C) Left circular polarization characterized by a rotatory manner of the electric field rotating counterclockwise. (D) Linear polarization with its electric field along the horizontal direction. First column is the vortex beams with no analyzer. Second column shows an analyzer set horizontally polarized. Third column shows an analyzer set vertically polarized

2.3 | Brain tissue preparation

The brain tissue samples were prepared following the procedures approved by the Institutional Animal Care and Use Committee (IACUC) of the City College of New York. A wild type adult mouse was anesthetized with isoflurane. After the mouse was completely anesthetized (confirmed with no response upon toe pinch), it was decapitated, and the brain was dissected and fixed in 4% paraformaldehyde overnight. The fixed brain was processed with coronal section by using a compresstome (VF300, Precision Instruments, Greenville, NC) at two different thicknesses (120 and 600 μm, respectively). The accuracy in tissue slice thickness was ±1 μm.

2.4 | Data collection and analysis

Data was collected for a 120 μm and a 600 μm thick brain tissues for linearly, circularly, radially, and azimuthally polarized beams at different positive ℓ values (ℓ = 0, 1, 3, 5

and 7), respectively. Also, the size of the OAM beam for each ℓ value was taken into account when sending it through each region of the brain sample. In the 120 μm thick tissue, the LG beam penetrated the cortex, the hippocampus, and white matter (Figure 1). The propagation of the LG beam is considered to be ballistic as the thickness of the sample results in a lack of scattering and interference in the trajectory of the LG beam, creating a straight path of travel [12]. In the 600 μm tissue, the LG beam penetrated the cortex and white matter (Figure 1). The propagation of the LG beam is considered to be diffusive as the increased thickness of the sample results in greater scattering of the LG beam [12]. Furthermore, a reference beam was also measured with no sample to take into account the change of incident light in calculating the transmittance. Finally, the data was analyzed using ImageJ software and by Eq. (12) as shown below:

$$\text{Transmitted intensity} = \frac{T_s}{T_{ns}} = 10^{-\text{OD}} = e^{\frac{-kz}{c}}, \qquad (12)$$

where T_s is transmitted intensity with sample, T_{ns} is the transmitted intensity with no sample, k is the transition probability, z is thickness of brain sample, and k/c is the absorption coefficient.

3 | RESULTS AND DISCUSSION

Figure 4 shows transmission difference between the cortex, white matter and hippocampus for a horizontally polarized collimated LG beam as a function of OAM with the tissue thickness of 120 μm. As shown below the transmittance after $\ell = 1$ in all targeted areas increases proportionately with ℓ. However, this increase is very small as the transmission ranged is about 6%.

Figure 5 shows transmission difference between the cortex and white matter for a horizontally polarized collimated
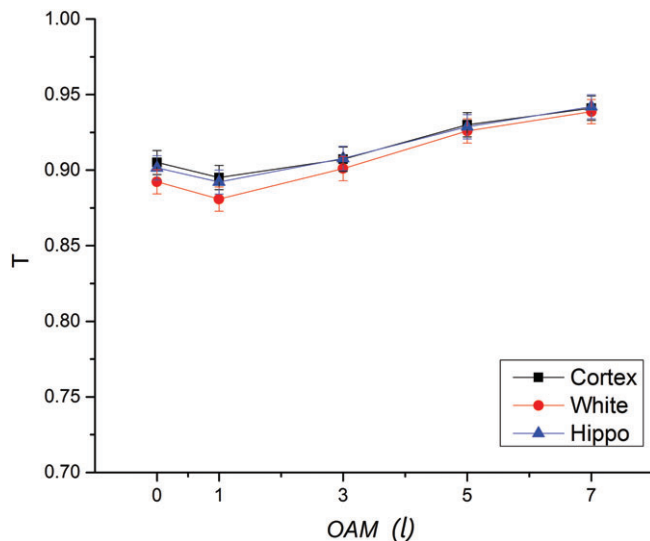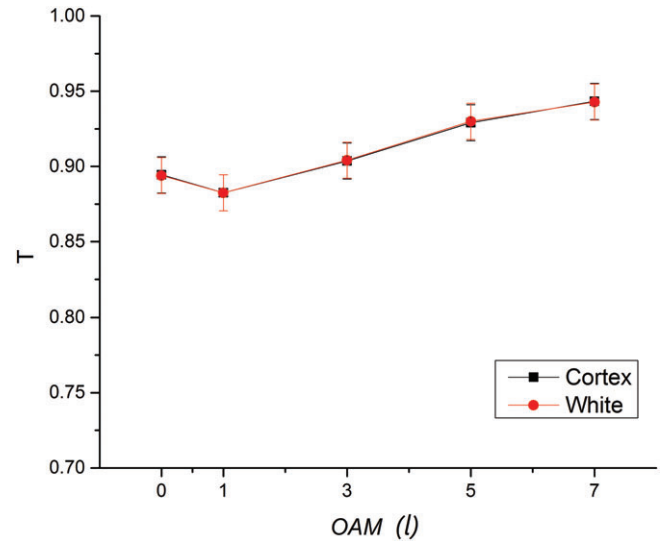

FIGURE 5 Transmittance (T) through a 600-μm sample as a function of OAM (ℓ) for a collimated horizontally polarized LG beam

LG beam as a function of OAM with the tissue thickness of 600 μm. In this case, the transmission range is also about 6%. These results further verify that the relationship between ℓ and transmittance of linearly polarized light through brain tissue is almost insignificant. In addition, this is theoretically proved by Forbes and Andrews [16] that linear polarization will have little to none chiroptical response from only OAM unlike circular polarization.

Figure 6 shows transmission difference between the cortex, white matter and hippocampus for a left circularly polarized collimated LG beam as a function of OAM with the tissue thickness of 120 μm. The transmittance of the beam generally increases as ℓ increases in all targeted parts. The sharpest increase in transmittance can be seen from $\ell = 3$ and above, in which all of the transmittance graphs share a similar curvature. Targeting the white matter consistently
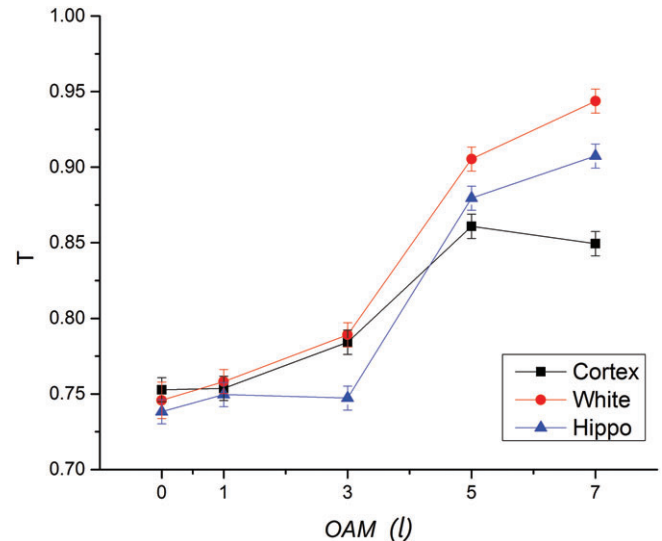

FIGURE 4 Transmittance (T) through a 120-μm sample as a function of OAM (ℓ) for a collimated horizontally polarized LG beam

FIGURE 6 Transmittance (T) through a 120-μm sample as a function of OAM (ℓ) for a collimated left circularly polarized LG beam
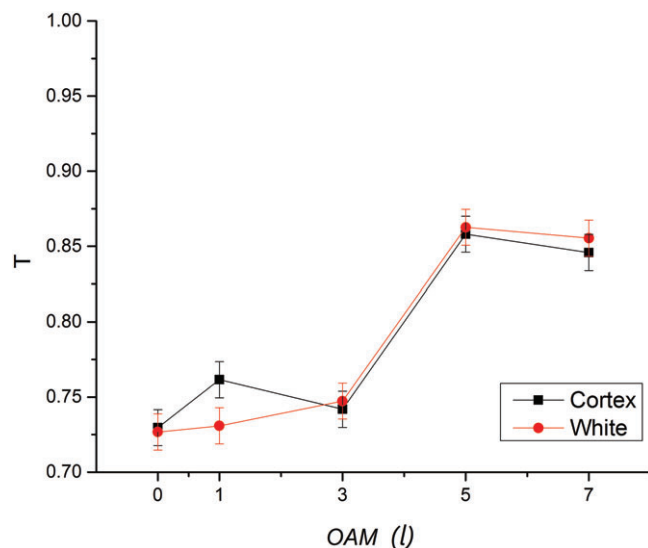
FIGURE 7 Transmittance (T) through a 600-μm sample as a function of OAM (ℓ) for a collimated left circularly polarized LG beam

yields the highest transmittance, whereas targeting the hippocampus yields the lowest transmittance from $\ell = 0$ to slightly before $\ell = 5$, and targeting the cortex yields the lowest transmittance from slightly greater than $\ell = 5$ onward. The overall transmission range achieved is about 20%.

Figure 7 shows transmission difference between the cortex and white mater for a circularly polarized collimated LG beam as a function of OAM with the tissue thickness of 600 μm. Figure 7 displays a similar, yet slightly weaker trend between ℓ and transmittance, as the graphs in Figure 6 and Figure 7 share similar curvatures and both display that a slightly higher amount of transmittance is achieved when targeting white matter versus targeting the cortex (specifically from $\ell = 3$ to $\ell = 7$). The overall transmission range
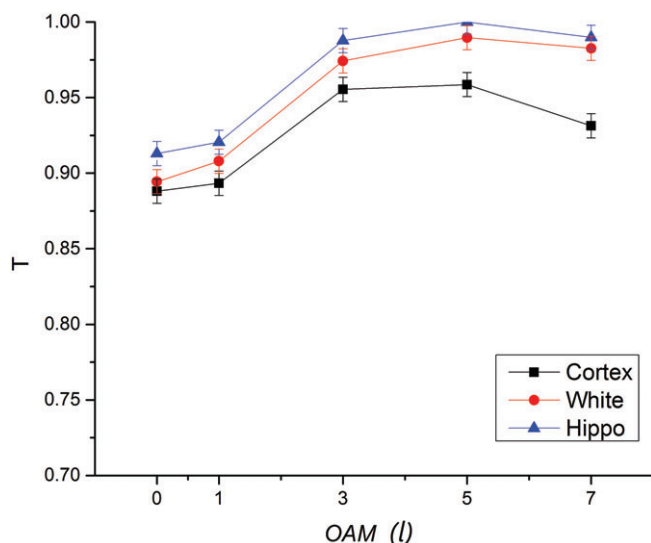

FIGURE 8 Transmittance (T) through a 120-μm sample as a function of OAM (ℓ) for a collimated radially polarized LG beam
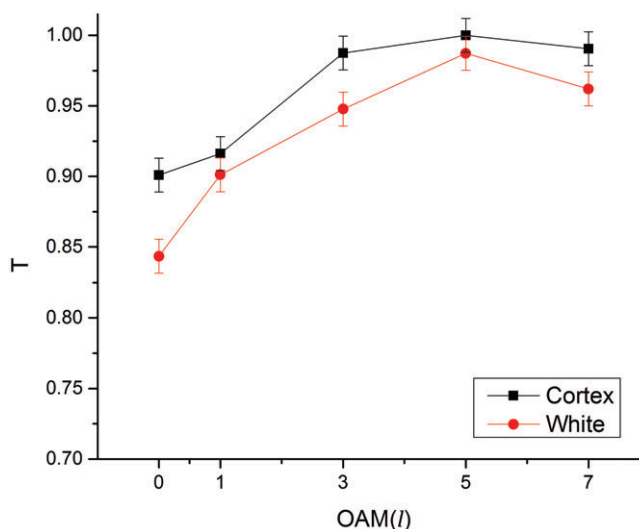

FIGURE 9 Transmittance (T) through a 600-μm sample as a function of OAM (ℓ) for a collimated radially polarized LG beam

achieved is about 14%. In addition, left circular polarization shows a high transmission range. This could be expected due to the interaction of the handedness of beam and the different values of the OAM [16].

Figure 8 shows transmission difference between the cortex, white matter and hippocampus for a radially polarized collimated LG beam as a function of OAM with the tissue thickness of 120 μm. The transmittance of the LG beam consistently increases as ℓ increases in all targeted regions and begins to wane as ℓ approaches 7. The sharpest increase is experienced from $\ell = 0$ to $\ell = 3$. Targeting the hippocampus consistently yields the highest transmittance while targeting the cortex consistently yields the lowest transmittance. The overall transmission range achieved is about 12%.

Figure 9 shows transmission difference between the cortex and white matter for a radially polarized collimated LG beam as a function of OAM with the tissue thickness of 600 μm. It shows a similar positive relationship between ℓ and the transmittance. Also the cortex shows a greater transmission than white matter. The overall transmission range achieved is about 16%. Moreover, radial polarization shows a high transmission range and well defined trend for each of the targeted regions. This is also expected due to the fact that radial is a superposition of left and right circular polarization.

Figure 10 shows transmission difference between the cortex, white matter and hippocampus for azimuthally polarized collimated LG beam as a function of OAM with the tissue thickness of 120 μm. The transmittance of the beam increases from $\ell = 1$ to $\ell = 7$. One difference that can be seen in all three regions is that from $\ell = 0$ to $\ell = 1$, only the transmittance for the cortex increases, while the transmittance for the white matter and hippocampus decreases. The overall transmission range achieved is about 14%.
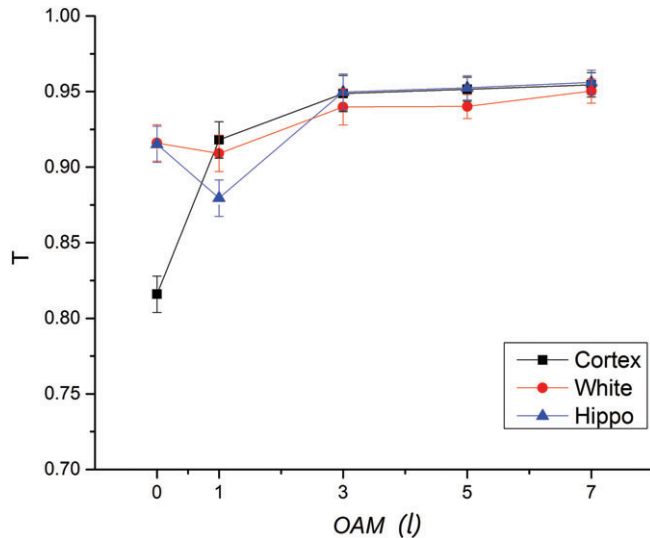
FIGURE 10 Transmittance (T) through a 120-μm sample as a function of OAM (ℓ) for a collimated azimuthally polarized LG beam

FIGURE 12 Cortex Region. Transmittance (T) through a 120-μm sample as a function of OAM (ℓ). LP, linear polarization; LCP, left circular polarization; AP, azimuthal polarization; RP, radial polarization

Figure 11 shows transmission difference between the cortex and white matter for azimuthally polarized collimated LG beam as a function of OAM with the tissue thickness of 600 μm. This figure shows a constantly higher transmission for cortex with respect to the ℓ values. In the case of white matter, the transmittance only increases from $\ell = 0$ to $\ell = 3$, after that the transmittance goes down. The overall transmission range achieved is about 13%. Additionally, azimuthal polarization shows a high overall transmission. Just like in the radial polarization case, this is also expected for azimuthal, being that is also made of left and right circular polarization.

3.1 | Data comparison between vector and scalar beams

Figures 12–14 show the transmission difference between the vector and scalar LG beams at three different (cortex, white
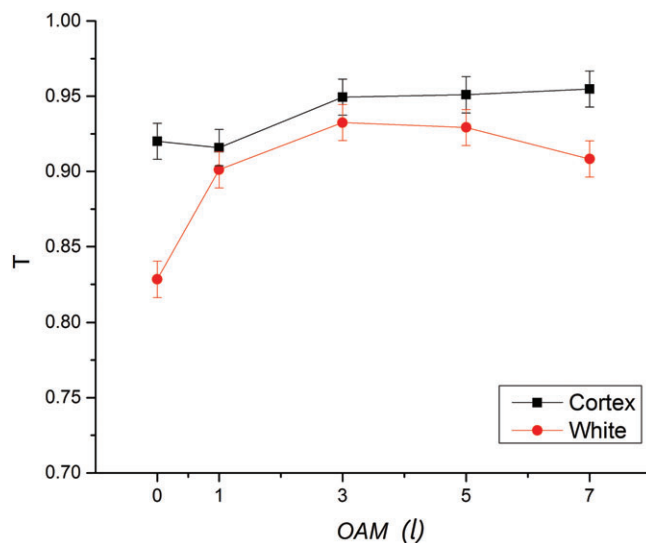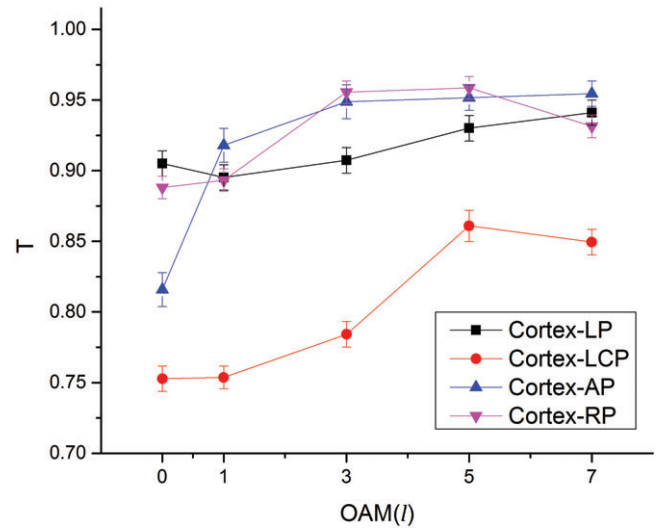
and hippocampus) 120 um brain regions (Ballistic). On these three graphs the vector beams show a higher transmission than the scalar beams. For example, azimuthal LG beams show a higher transmission difference for the cortex region (Figure 12); and the radial polarized LG beams, show a significant higher transmission for the white and the hippocampus region (Figure 13, Figure 14). Moreover, referring to the scalar beams, the left circular polarized LG beams show a higher constant increase of transmission as we increase the ℓ values, specially for the white region (Figure 13). However linear polarized LG beams show a small transmission difference; although, its transmission goes above the left circular polarization.
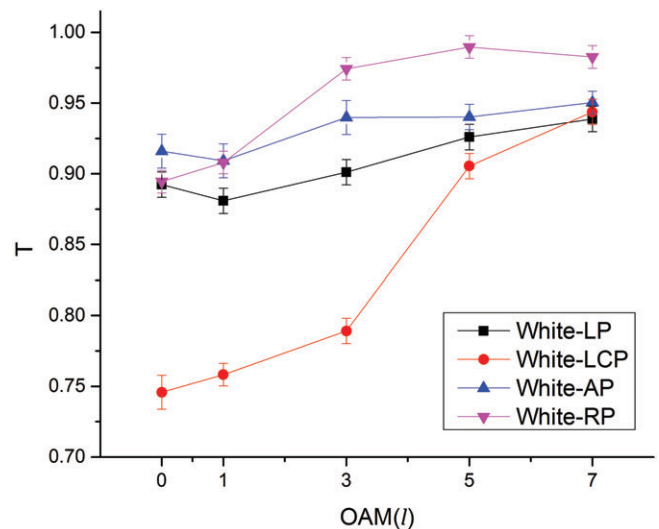

FIGURE 11 Transmittance (T) through a 600-μm sample as a function of OAM (ℓ) for a collimated azimuthally polarized LG beam

FIGURE 13 White Region. Transmittance (T) through a 120-μm sample as a function of OAM (ℓ). LP, linear polarization; LCP, left circular polarization; AP, azimuthal polarization; RP, radial polarization
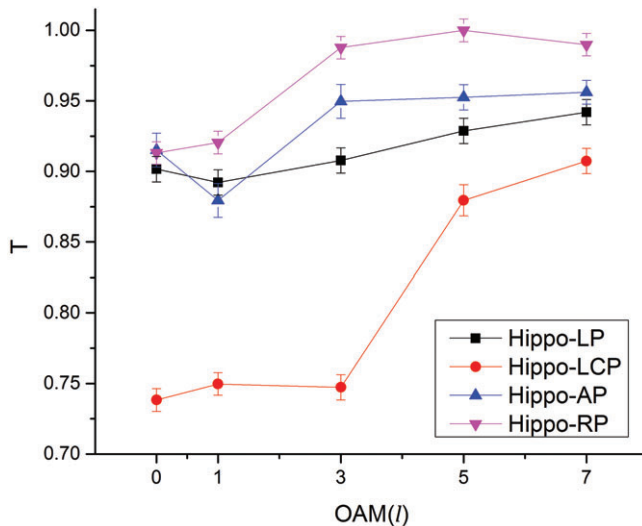
FIGURE 14 Hippocampus Region. Transmittance (T) through a 120-μm sample as a function of OAM (ℓ). LP, linear polarization; LCP, left circular polarization; AP, azimuthal polarization; RP, radial polarization

FIGURE 16 White Region. Transmittance (T) through a 600-μm sample as a function of OAM (ℓ). LP, linear polarization; LCP, left circular polarization; AP, azimuthal polarization; RP, radial polarization

Figures 15 and 16 show the transmission difference between the vector and scalar LG beams at two different (cortex and white) 600 um brain regions (Diffusive). On these two graphs both vector beams show a higher transmission compared to the scalar beams; particularly on both regions, the radial LG beams show a constant increase as the ℓ values increase, which is more significant than the other vortex beams. Additionally, for the white region (Figure 16) the azimuthal LG beams show a better overall transmission difference than the linear beams do. Moreover, the linear polarized LG beams show a constant increase of transmission for larger ℓ values, but a small overall transmission difference; although, it is observed the same transmission difference as the azimuthal beams for the cortex region (Figure 15). On the other hand, the left circular polarized LG
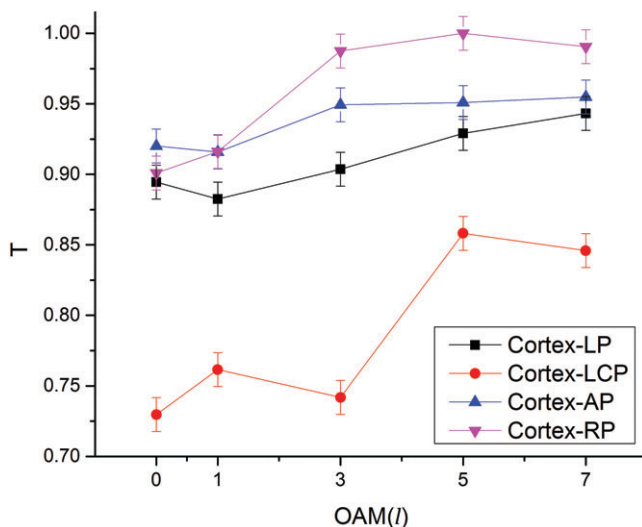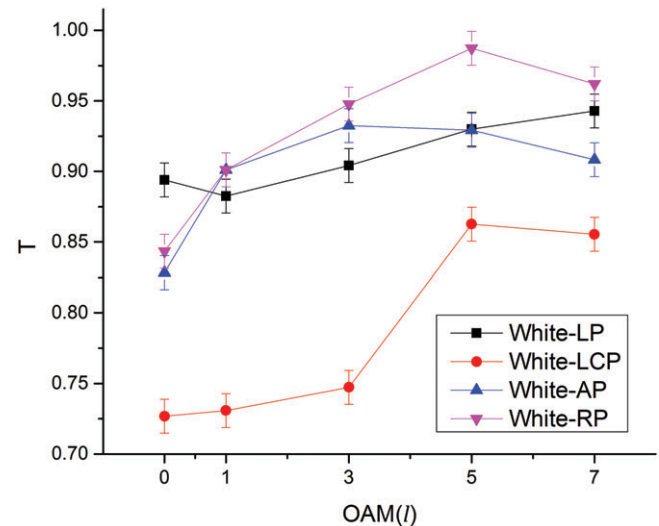
beams show an unstable increase of transmission for the cortex region (Figure 15), but a more constant increase of transmission for the white region (Figure 16); although, do not increase as high as the vector beams or linear beams.

4 | CONCLUSION

Our vector beam study produced the salient outcome that the transmittance of LG beams through brain tissue displays strong positive dependency on OAM for collimated, radially, azimuthally and left circularly polarized LG beams.

The classical entangled beam of radial and azimuthal polarization gave highest transmission as the ℓ values increase in both ballistic and diffusive regions. Also, these vector beams gave clear trends when targeting different areas of the brain at the ballistic and diffusive region. Furthermore, radial polarization gave the highest transmission range at the diffusive region, while left circular polarization showed the highest transmission for the ballistic region. Moreover, in targeting the hippocampus, cortex, and white matter, radially polarized light proved to be the most effective followed by azimuthal polarized beams. On the other hand, linearly polarized light showed positive dependence on ℓ, but this dependence proved to be less significant in comparison to the dependences on the other tested polarizations. Hence, these results support the idea that light transmission through different areas of the brain varies. Still, future studies need to be conducted to further validate this conclusion.

Moreover, these results allow for the optimization of optical brain imaging depending on which area of the brain must be targeted. For example, by targeting specific regions affected by neurodegenerative diseases, we are able to understand and learn more about the mystery behind these

FIGURE 15 Cortex Region. Transmittance (T) through a 600-μm sample as a function of OAM (ℓ). LP, linear polarization; LCP, left circular polarization; AP, azimuthal polarization; RP, radial polarization

diseases with the aim of preventing or treating it. Also, the use of this imaging method at different brain regions will differentiate an abnormal brain tissue from a normal one. For a future project we plan to do brain transmission and imaging on a human brain with Alzheimer's disease, focusing on areas that are mainly affected such as hippocampus, cingulate gyrus, and amygdala [36]. In addition, Forbes and Andrews [15–18] showed dipole and quadrupole have a chiroptical effect associated with OAM with circular dichroism (left and right circular polarization). Afanasev et al. [37] have shown that higher multipole transitions exhibit circular dichroism with OAM (ℓ) dependency, in non-chiral atomic matter.

Furthermore, our future study will compare single photons in quantum entanglement (Q-ons) and classical entanglement (C-ons) at high photon flux; in particular, on radial and various vector spatial and polarization beams for improving imaging in tissue. This study will be further extended for breast tissue as well. These types of imaging methods can hopefully pave the way to improve mental disorder and breast cancer treatment, and shine light on C-ons in the brain.

ORCID

Robert Alfano http://orcid.org/0000-0001-5418-0404

REFERENCES

[1] K. M. Yoo, R. R. Alfano, *Opt. Lett.* **1990**, *15*, 320.
[2] L. Shi, L. A. Sordillo, A. Rodrígues-Contreras, R. Alfano, *J. Biophotonics* **2016**, *9*, 38.
[3] X. Ni, R. R. Alfano, *Opt. Lett.* **2004**, *29*, 2773.
[4] P. Shumyatsky, G. Milione, R. R. Alfano, *Opt. Comm.* **2014**, *321*, 116.
[5] L. Allen, M. W. Beijersbergen, R. J. C. Spreeuw, J. P. Woerdman, *Phys. Rev. A* **1992**, *45*, 8185.
[6] B. Ndagano, B. Perez-Garcia, F. S. Roux, M. McLaren, C. Rosales-Guzman, Y. Zhang, O. Mouane, R. Hernandez-Aranda, T. Konrad, A. Forbes, *Nat. Phys.* **2017**, *13*, 397.
[7] G. Milione, T. A. Nguyen, D. A. Nolan, E. Karimi, S. Slussarenko, L. Marrucci, R. R. Alfano, OSA Technical Digest, Optical Society of America, *Front. Opt.* **2013**, paper FM3F.4.
[8] G. Milione, H. I. Sztul, D. A. Nolan, R. R. Alfano, *Phys. Rev. Lett.* **2011**, *107*, 053601.
[9] G. Milione, S. Evans, D. A. Nolan, R. R. Alfano, *Phys. Rev. Lett.* **2012**, *108*, 190401.
[10] G. Milione, T. A. Nguyen, J. Leach, D. A. Nolan, R. R. Alfano, *Opt. Lett.* **2015**, *40*, 4887.
[11] C. Sun, Z. Chen, J. Pu, *Acta Opt. Sin.* **2014**, *34*, 0601002.
[12] R. R. Alfano, W. B. Wang, L. Wang, S. K. Gayen, in *Photonic, Scientific Foundations, Technology and Applications*, Vol. IV (Ed: D. Andrews), John Wiley, Hoboken, New Jersey **2015**, p. 369.
[13] K. M. Yoo, F. Liu, R. R. Alfano, *Phys. Rev. Lett.* **1990**, *64*, 2647.
[14] M. Zamorano, H. Torres-Silva, *Phys. Med. Biol.* **2006**, *51*, 1661.
[15] K. A. Forbes, D. L. Andrews, *Proc. SPIE 10549, Complex Light and Optical Forces XII* **2018**, p. 1054915.
[16] K. A. Forbes, D. L. Andrews, *Proc. SPIE 10672, Nanophotonics VII* **2018**, p. 1067210.
[17] D. L. Andrews, *J. Opt.* **2018**, *20*, 033003.
[18] K. A. Forbes, D. L. Andrews, *Opt. Lett.* **2018**, *43*, 435.
[19] M. A. J. Silva, *Sci. Am.* **2017**, *317*, 30.
[20] R. D. Fields, *Science* **2010**, *330*, 768.
[21] L. Shi, L. Lindwasser, W. Wang, R. R. Alfano, A. Rodriguez-Contreras, *J. Biophotonics* **2017**, *10*, 1756.
[22] L. Shi, E. J. Galves, R. R. Alfano, *Sci. Rep.* **2016**, *6*, 37714.
[23] M. Le Bellac, *Quantum Physics*, Cambridge University, Cambridge **2016** Chap 3, and 6.
[24] H. Sroor, N. Lisa, D. Naidoo, I. Litvin, A. Forbes, *Phys. Rev. Appl.* **2018**, *9*, 044010.
[25] B. Ndagano, I. Nape, M. Cox, C. Rosales-Guzman, A. Forbes, *J. Lightwave Tech.* **2018**, *36*, 292.
[26] S. Matsuo, *Opt. Express* **2011**, *19*, 12815.
[27] S. Mamani, E. Bendau, J. Secor, A. Solyman, J. Tu, R. R. Alfano, *Appl. Opt.* **2017**, *56*, 1.
[28] C. Kittel, *Quantum Theory of Solids*, John Wiley, New York **1964** Chap 3 and 4.
[29] R. Alfano, *J. Opt. Soc.* **1970**, *60*, 66.
[30] S. Kumar, K. Boone, J. Tuszyński, P. Barclay, C. Simon, *Sci. Rep.* **2016**, *6*, 36508.
[31] S. Herculano-Houzel, B. Mota, R. Lent, *PNAS* **2006**, *103*, 12138.
[32] N. Gilani, Six Types of Neuroglia, https://sciencing.com/six-types-neuroglia-6302092.html (accessed: May 2018).
[33] S. E. Lyshevski and G. R. Tsouri, *Nanotechnology (IEEE-Nano), 11th IEEE Conference* (**2011**).
[34] M. Rahnama, J. A. Tuszynski, I. Bókkon, M. Cifra, P. Sardar, V. Salari, *J. Integr. Neusci.* **2011**, *10*, 65.
[35] M. Jibu, S. Hagan, S. R. Hameroff, K. H. Pribram, K. Yasue, *Biosystems* **1994**, *32*, 195.
[36] A. J. Silva, *Sci. Am.* **2017**, *317*, 32.
[37] A. Afanasev, C. E. Carlson, M. Solyanik, *J. Opt.* **2017**, *19*, 105401.